Integrating perovskite materials and bamboo-based activated carbon for electrochemical energy storage in hybrid supercapacitors

Ricardo Martínez[1,3], Edwin Cruz[1,3], Shawn Zografos[1,3], Joesene Soto[2,3], Ratnakar Palai[1,3], Carlos Cabrera[4]

[1]Department of Physics, University of Puerto Rico, Rio Piedras, San Juan, PR, 00931, USA

2. Department of Chemistry, University of Puerto Rico, Rio Piedras Campus, San Juan, PR, 00931, USA

3. Center for Interfacial Electrochemistry of Energy Materials, University of Puerto Rico

4. Department of Chemistry and Biochemistry, University of Texas, El Paso, TX, 79968, USA

Abstract:

Electrochemical devices such as fuel cells, lithium-ion batteries, and supercapacitors have become vital emerging technologies for conserving, storing, and transferring energy. Electrochemical supercapacitors are an alternative for energy storage devices that can satisfy the demand for a high-power supply and long cycling life. However, the low energy density and high manufacturing cost are issues that limit their further development. Here, we -report the innovative integration of perovskite (LSMO, BTO, and PZT) and activated carbon materials deposited in a thin layer by the spray pyrolysis technique to hybridize the double-layer electrode and the electroactive medium in electrochemical supercapacitors. Different supercapacitor configurations, in the form of asymmetric coin cells using organic cellulose and cotton lint as separators, were –assembled and tested to investigate their dynamic electrical behavior and performance for power applications through cyclic voltammetry, galvanostatic charge/discharge profiling, electrochemical impedance spectroscopy, and modeling of the experimental data. The fabricated supercapacitor device with BTO/cellulose achieved the specific capacitances of 300 F/g, energy densities of 6.7 Wh/kg, power densities of 600 W/kg, and maintain more than 95% of the initial capacitance after several charge/discharge cycles. Based on these promising properties, two identical supercapacitor cells were arranged in series and used to power a yellow LED for several minutes, confirming that our supercapacitor approach exhibits potential for practical applications. This work -will facilitate the realization of more flexible, light, and inexpensive -supercapacitors with the potential for long life and capable energy-storing performance.

Keywords

Supercapacitor, energy storage, activated carbon, perovskite materials, electrochemical studies, ferroelectrics, spray pyrolysis.

1. Introduction

The need for new energy alternatives is urgent in the modern world. Developing new energy storage devices can meet the demand. However, there is a challenge to achieve -high efficiency. Nowadays, there is a tireless search for new and more multifunctional materials that allow more efficient energy storage technologies [1]. Electrochemical devices, such as fuel cells, lithium-ion batteries, and supercapacitors have become vital emerging technologies for conserving, storing, and transferring energy. Although these devices continue to develop rapidly in terms of cost and performance, the materials that make them up are still a great challenge to optimize [2]. Electrochemical supercapacitors are an alternative for energy storage devices that can satisfy the demand for a high-power supply and long cycling life. However, the low energy density and high manufacturing cost are issues that limit their further development. In addition to the development of the material for the electrodes in supercapacitors, many research groups around the world are working other crucial parts such as electrolyte, separator, and dielectric medium, which are required to significantly improve the specific capacitance of supercapacitors [3,4]. The perovskite materials with the general formula ABO_3 (A trivalent or divalent cation and B divalent or tetravalent cation) have found applications in energy storage systems since they can be used as electrodes [5-9], solid-state electrolytes [10], and electroactive dielectrics for supercapacitors [11-13]. Supercapacitors are a category of electrical condenser based on the properties of charge distribution on the interface of an electrode-electrolyte solution. The performance of supercapacitors has improved from understanding the charge energy storage mechanisms and developing advanced nanostructured materials [14]. The energy storage of a supercapacitor is mainly based on the accumulation of charge through electrochemical conversion [15], which can offer elevated power densities, elongated cycle life, quick charge, and discharge time intervals, as well as being a clean and safe means of energy [16]. Electrochemical energy storage can be achieved from electrostatic interactions in electrochemical double-layer capacitors (EDLCs) or via redox reactions of electrode materials during the charging/discharging process, as in pseudocapacitors [17]. To elevate the capacitance and energy storage capability, combining EDLC and pseudocapacitors in a hybrid supercapacitor allows higher power and energy densities than the normal EDLC or a simple pseudocapacitor [18]. Compared to other energy-storing devices such as fuel cells and batteries, hybrid supercapacitors can hold greater power density but low energy density [19]. On the other hand, hybrid supercapacitors can yield much higher specific capacitance than conventional capacitors [20]. Given that the attributes of any supercapacitor are their energy stored and maximum instantaneous power [21], these properties are closely related to the capacitance or ratio of stored charge at each interface C (F), the applied voltage V (V), and internal or equivalent series resistance R_s (Ω) according to Eq. (1) and Eq. (2) below:

$$E = \frac{1}{2}CV^2 \qquad (1) \qquad P_{max} = \frac{V^2}{4R_s} \qquad (2)$$

To overcome the obstacle of low energy density in hybrid supercapacitors, it becomes necessary to improve two things: (i) the total capacitance and (ii) the cell voltage. Several intensive and advanced approaches exist to fit these needs for developing new materials and an improved understanding of ion transport mechanisms. The capacitance can be enhanced through the hybridization of electrode materials (*e.g.*, metal oxides) by adding electrochemically active materials due to their high surface area and porous structure (*e.g.*, activated carbon) [22,23] or by the introduction of redox additives into the conventional electrolytes with additional pseudocapacitance contribution between electrolyte and electrode[24,25]. The cell voltage can be enhanced by combining asymmetric electrodes with EDLC and the redox reactions of electroactive materials [26-29]. Since the maximum energy storage is achieved when the cell voltage is at

a maximum, which is usually limited by the breakdown strength of the dielectric. It is necessary to consider other factors such as the resistance of internal components of the capacitor, the effective surface area of electrodes, the dielectric thickness, and electrolyte stability. Although, it has not been easy to circumvent all these issues at the same time, hybrid supercapacitors of electrochemical behavior based on new materials have demonstrated that they can lead to an increase in both capacitance and energy by a factor of around 10,000 more than those achievable by regular capacitors. [30-34]. Researchers around the world are working on the phase synthesis of these materials at comparatively lower temperatures by utilizing methods such as co-precipitation [35,36], nanocasting [37,38], sol-gel [39,40], hydrothermal [41,42], combustion [43,44], spray pyrolysis [45-48], thermal decomposition [49] and so on. Among the various methods used, spray pyrolysis (SP) is a versatile technique extensively used to grow electrodes and electroactive materials in thin/thick films for supercapacitor applications [50]. SP is a simple, fast, and continuous deposition method in the aerosol processes. The stoichiometry and morphology of the film can be tuned by controlling some parameters, for example, concentration of the precursor, substrate temperature, and the rate of spray. The application of SP in the industry is very promising owing to the low running cost and possibility of deposition in large areas [51]. In this work, we report results on the study and development of electrochemical supercapacitors based on the hybridization of electrochemically and electrostatically charged storage from perovskite materials. Previously, we have reported the fabrication and feasibility of several perovskite materials with excellent dielectric, ferroelectric, ferromagnetic, and multiferroic properties for multifunctional applications (*e.g.*, high dielectric capacitors, non-volatile ferroelectric random-access memories, gas sensors, optoelectronics, spintronics, photovoltaic cells, energy storage devices and so on) [52-56]. In the present work, we synthesized the perovskite transition metal oxide $La_{0.85}Sr_{0.15}MnO_3$ (LSMO), which has low resistance at high specific capacitance [57-60] and it has been blended with porous and high surface area activated carbon (AC) [61-63] to be used as electrode material, and also high dielectrics/ferroelectrics perovskites such as $PbZr_{0.52}Ti_{0.48}O_3$ (PZT) [64] and $BaTiO_3$ (BTO) [65,66] to be used as electroactive media in the assembly of low-cost coin cell supercapacitor (CCSC) devices for energy storage. These materials' structural, porous characteristics, electrical, and electrochemical properties were investigated before manufacturing and evaluating the CCSC devices. The spray pyrolysis method was used to architect a heterogeneous and flexible layered structure of electrodes and dielectrics on aluminum (Al) and copper (Cu) substrates. Cellulose and cotton fabric lint soaked in an aqueous electrolyte were used as separator layers to complete the CCSC devices. A performance comparison of the tested CCSS devices was also carried out. The knowledge gained in this research could provide valuable guidance for further developing supercapacitors with high-performance and stable anion-intercalation-type perovskite materials.

2. Material and methods

2.1. Synthesis of $La^{3+}_{0.85}Sr^{2+}_{0.15}(Mn^{3+}_{0.85}Mn^{4+}_{0.15})O^{2-}_3$

The synthesis of strontium-doped lanthanum manganite perovskite $La^{3+}_{0.85}Sr^{2+}_{0.15}(Mn^{3+}_{0.85}Mn^{4+}_{0.15})O^{2-}_3$ (LSMO) followed a solid-state procedure like that used for other metal oxide powder perovskites [35-38]. The process involved the mixture of high purity (~ 99.9 %) raw materials, La_2O_3, $SrCO_3$, Mn_2O_3 and MnO_2, in isopropyl alcohol media with the appropriate amounts based on the stoichiometric ratios of La:Sr:Mn = 0.85:0.15:1. The resulting powder was further heated at 1000 °C for 6 hours and then re-heated at 1200 °C for 4 hours to induce a good powder crystallization and a single-phase perovskite structure.

2.2. *Synthesis of $Pb^{2+}Zr^{4+}_{0.52}Ti^{4+}_{0.48}O^{2-}_{3}$*

The lead zirconate titanate perovskite $Pb^{2+}Zr^{4+}_{0.52}Ti^{4+}_{0.48}O^{2-}_{3}$ (PZT) was also synthesized by conventional solid-state route [64]. The raw materials in powder oxide form of high purity: PbO (99%), TiO_2 (99.4%), and ZrO_2 (99.7%) were homogenized in isopropyl alcohol as milling media with the appropriate Zr: Ti ratio. Excess of 10 mol% of PbO was added to the stoichiometric composition to avoid lead deficiency during synthesis and ensure higher densification. The resulting mixture was dried and ground with mortar to break the agglomerates. Then, the powder was calcinated at 850 °C for 6 hours and re-heated at 875 °C for 4 hours to induce a good powder crystallization and a single-phase solid perovskite structure.

2.3. *Synthesis of $Ba^{2+}Ti^{4+}O^{2-}_{3}$*

Barium titanate perovskite $Ba^{2+}Ti^{4+}O^{2-}_{3}$ (BTO) was synthesized by sol-gel method [65]. High purity (>99.9 %) barium acetate $Ba(OOCCH_3)_2$ and titanium (IV) isopropoxide $Ti[OCH(CH_3)_2]_4$ were used as precursors. Both precursors were dissolved in glacial acetic acid under constant magnetic stirring for 1 hour to 60 °C. Ethylene-glycol was slowly added to obtain a uniform and transparent gel. The gel was filtrated as a stock solution and was then completely dried. Later, the agglomerates were broken up manually until a fine powder. The powder was calcined at 400 °C for 4 hours to eliminate organic residues, and then to 950 °C for 5 hours and re-heated at 1000 °C to induce a good powder crystallization and a single-phase perovskite structure.

2.4. *Synthesis of activated carbon*

An activated carbon was prepared from moso bamboo culms (Phyllostachys edulis), which were, in turn, ground and sieved to get a fine sawdust. The sawdust was thermochemically decomposed by pyrolysis under a nitrogen atmosphere to 650 °C until it got bamboo charcoal (BC). Then, the BC was chemically activated using H_3PO_4. Subsequently, the BC was thermally treated from room temperature to 750 °C in the nitrogen atmosphere. The resulting bamboo-activated carbon (BAC) was washed with distilled water until neutral pH. The BAC was finally dried, ground, and sieved into a fine powder

2.5. *Structural and microstructural characterization*

A Rigaku SmartLab X-ray diffractometer with Cu-K α(λ = 1.5046 Å) radiation was used to examine the structural properties of perovskites and carbonaceous samples. The perovskite's phase composition was identified by comparing the experimental patterns with ICDD and ICSD database structures. A JEOL JEM 2001 scanning electron microscopy equipped with coupled energy dispersive X-ray spectroscopy (EDX) examined all samples' morphology, particle size, and elemental composition.

2.6. *Porous structure of activated carbon*

From adsorption isotherm measurements, using a TriStar II 3020 V1.01 equipment at nitrogen liquefaction temperature (77.35 K), it was possible to calculate the specific surface area and porosity structure of the activated carbon according to the Brumaire-Emmett-Teller (BET) and the Barrett–Joiner–Halenda (BJH), respectively.

2.7. Electrical characterization of electrodes

The electrical performance of LSMO and LSMO+BAC pellets in the form of two-electrode capacitor configuration with an area of 1.23 cm^2 and metalized on both sides with silver paint, was evaluated by ac impedance spectroscopy at room temperature at the frequency range between 1 Hz to 1 MHz and ac voltage of 10 mV using an automated HIOKI 3522/3532-50 LCR HiTester

2.8. Electrochemical characterization of electrodes

LSMO and 4:1 LSMO + BAC powders were prepared for testing electrodes. A small amount of 32 mg of each of these powders was added and homogenized separately in 1 ml of a solution consisting of 2:1:1:0.1 ethanol, isopropanol, water, and nafion (5% in ethanol), respectively. Then, an aliquot of 5 µL of the LSMO and LSMO + BAC inks was glued to the surface of an ultra-polished glassy carbon electrode with a geometric surface area of 0.07068 cm^2. Finally, three-electrode configurations were assembled in a glass cell using the previously mentioned materials as working electrodes, an Ag/AgCl as a reference electrode, and a Pt wire as the counter, and immersed in a 1 M KOH solution used as electrolyte. The electrochemical performance of LSMO and LSMO+BAC electrodes was evaluated by cyclic voltammetry (CV) curves at scan rates ranging between 10 and 100 mV/s, and galvanostatic charge/discharge (GCD) profiles at constant current were carried out using a potentiostat (Autolab PGSTAT 30) station.

2.9. Electrical characterization of electrodes

LSMO and LSMO+BAC pellets, with an area of 1.23 cm^2 and metalized on both sides with silver paint, were tested as capacitors. The electrical performance of these capacitors was evaluated by AC impedance spectroscopy at room temperature at the frequency range between 1 Hz to 1 MHz and AC voltage of 10 mV using an automated HIOKI 3522/3532-50 LCR HiTester.

2.10. Ferroelectric characterization of PZT and BTO

Room temperature measurements of hysteresis loops (polarization) vs. (electric field) for ferroelectrics BTO and PZT were carried out by using a ferroelectric workstation Radiant Technologies Hysteresis Loop Tester (RT6000HVS) at a unipolar mode.

2.11. Spray pyrolysis

Our approach for fabricating electrochemical supercapacitors required the systematical deposition of films using the spray pyrolysis (SP) process. Figure 1 illustrates the spray pyrolysis setup for manufacturing substrate/electrode/dielectric films. First, we prepared a polymeric solution with 1g of polyvinylpyrrolidone (PVP 1.2 g/cm^3, MW ~1,300,000) dissolved in 10 ml of isopropyl alcohol by a magnetic stirrer at 60 °C until ensuring the dissolution of PVP. Then, 1g of LSMO powder blended with BAC with molar ratios of 4:1 was added to the polymeric solution and further magnetically stirred for 1 hour at room temperature, followed by sonification to form a homogeneous ink for the growth of electrodes. Second, we prepared 10 ml of polymeric solution, added 2 g of ferroelectric powder (PZT or BTO), and further magnetically stirred for 1 hour at room temperature, followed by sonification to form a homogeneous ink for the growth of electroactive media. Then, we loaded the electrode ink into an airbrush (model Paasche TG Talon). High-purity aluminum and copper sheets (95 mm x 95 mm x 40 mm) were used as substrates and carefully kept on a hot plate at 80 °C. The distance between the spray nozzle (0.38 mm diameter) and the substrates was adjusted to 15 cm so that the aerosol droplets reached the

substrate in fine mist. Then, each substrate was coated with 5 ml of ink using the airbrush under a set pressure of 40 PSI, given a constant flow rate of ~ 0.8 ml/min. Once the deposition is over, each substrate is left to dry for 24 hours. We repeated this process, loading the dielectric ink in the airbrush to coat the electrode layer. In the end, we got flexible films with a thickness of ~200 mm on the metal substrates.

2.12. Architecture and assembly of coin cell supercapacitor (CCSC) devices

In order to understand the understand and enhance the supercapacitors performance, we fabricated four supercapacitors with different configurations. The details of assembled four supercapacitors are as follow. The LSMO+BAC/dielectric films coated copper and aluminum substrates were cut into circular sheets with diameters of 10 mm and a surface area of 0.8 cm^2 using a metal hole puncher. For the two-electrode configurations Cu used as cathode, while Al as anode as per their reduction potential. The LSMO+BAC/dielectric heterostructure film had a loading mass of ~ 20 mg. A synthesized polymer gel solution, prepared by adding PVP powder (0.2 g), isopropyl alcohol (10 ml), and H_3PO_4 (0.5 ml) to distilled water (30 ml), was used as electrolyte. Cotton lint fabric and self-made cellulose membranes, whose diameter, thickness, and mass were 15 mm, ~ 200 mm, and ~ 27 mg, respectively, were used as separator layers. Each separator layer was well-wetted in 100 mL of the electrolyte before being sandwiched between electrodes. Then, we fixed the material setup into hermetic sealed coin cell cases (CR2032/SS304 20d x 3.2t mm) under a constant spring pressure of 20 kg to ensure electrical contact. Figure 2. shows the architecture and assembly of such electrochemical cell coin supercapacitors.

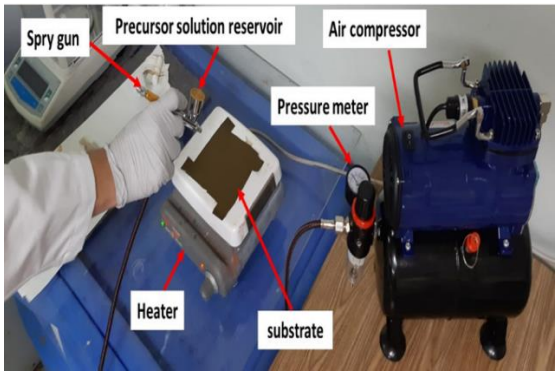

Fig. 1. Spray pyrolysis technique to fabricate metal/electrode/dielectric layers for electrochemical SCs.

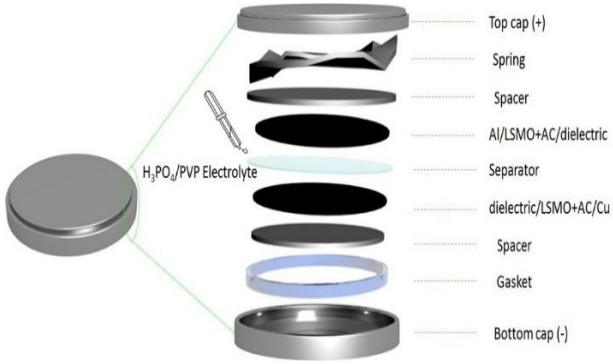

Fig. 2. Architecture and assembly of perovskite-based electrochemical coin cell SC.

2.13. Electrochemical characterization of CCSC devices

The electrochemical characterization of CCSC devices was carried out using the SP-200 potentiostat by BioLogic instruments. The characterization consists of electrochemical impedance spectroscopy (EIS), cyclic voltammetry (CV), and galvanostatic charge-discharge (GCD) based on a two-electrode system. The EIS study was conducted over a frequency range of initial and final values of 1 MHz and 0.01 mHz, respectively. CV analysis was conducted in the potential window of 0-0.4 V, and scan rates between 10 and 120 mV/s. GCD analysis was conducted using 100 charge/discharge cycles at a potential of 0-0.4 V and 100 mV/s.

3. Results and discussion

3.1. Structural analysis of perovskites and carbonaceous materials

Fig. 3 shows the phase structure, conducted by X-ray diffraction (XRD), of LSMO, BTO, and PZT (-a) and carbonaceous BC and BAC powders (-b). LSMO, BTO, and PZT showed the existence of high-purity phases with the formation of perovskite structures. We found that the crystal structure and the XRD patterns match well with the standard XRD ICDD (JCPDS) cards or ICSD collections. According to these databases, the LSMO structure is indexed to an orthorhombic phase with lattice parameters equal to a = 5.5373 Å, b = 5.5023 Å, and c = 7.7853 Å, ICDD # 01-072-7940 [67]; BTO is indexed to a tetragonal phase with lattice parameters equal to a = 3.994 Å, b = 3.994 Å, and c =4.034 Å, ICSD # 37459 [68]; and PZT is indexed to a tetragonal phase with lattice parameters equal to a = 4.0406Å, b = 4.0406 Å, and c = 4.1290 Å, ICDD # 33-0784 [69]. Regarding the BC XRD pattern, it exhibited two broad reflections at 2θ= 24º (002) and 44º (101) that are typical of a graphite structure. The appearance of the peak at around 24° signifies an increasing regularity of crystalline structure, which indicates a better layer alignment. The structure of BC can be assigned to that of the hexagonal structure in concordance with the ICDD card # 7740-44-0 [70]. We can see that with the H_3PO_4 activation process, both peaks of BC disappeared, and many defects emerged in the lattice, likely due to the intercalation of P and the evaporation of C. The new reflections on the BAC structure have low intensity and can be assigned to the formation of carbonates and phosphates due to the small amounts of Na, P, Si, S, K, and Mg found in the BAC EDX spectrum. These impurities phases were identified and marked in the XRD pattern (inset Fig. 3 right).

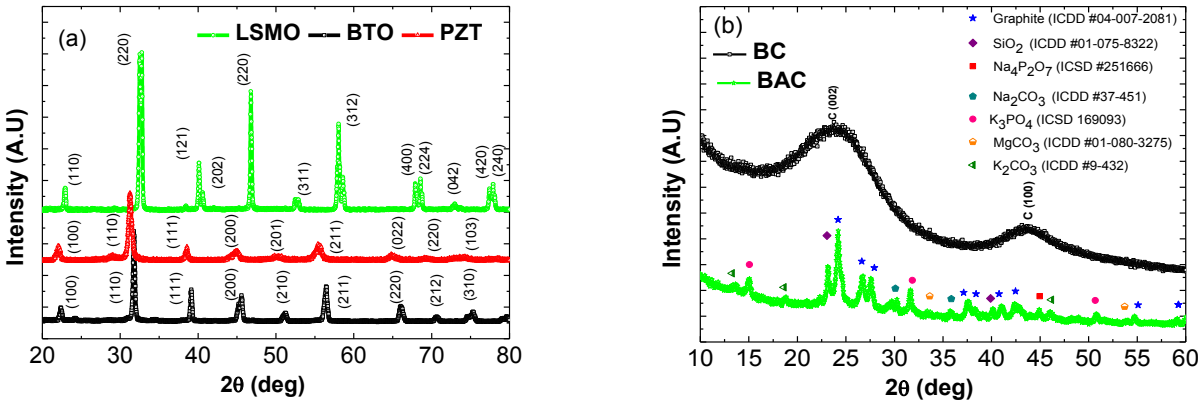

Fig. 3. X-ray diffraction pattern of LSMO, BTO, PZT (a), BC, and BAC samples (b). The phases of impurities in BAC are shown by symbols.

3.2. Elemental composition

The elemental and chemical composition of the samples was analyzed using energy dispersive x-ray spectroscopy (EDX). Fig. 4 shows the elemental and chemical composition of LSMO, PZT, BTO (let), and BAC (right). EDX measurements confirmed the existence of elements and chemical compositions in all perovskites and carbonaceous material. However, the chemical composition of BAC contains trace elements such as P, Na, K, Si, S, and Mg on its porous surface in the form of agglomerates. The inset in Fig. 4 right shows an agglomerate of ~1.3 μm. The presence of P is mainly from the phosphoric acid used for the activation. However, it is noteworthy that the bamboo composition is endowed with these minerals [71]. Despite that, the BAC was well washed after activation to remove ions, salt, or remaining compounds; it is possible to obtain secondary phases due to the thermal treatment at high temperatures.

This result corroborates the activated carbon diffraction pattern where the crystalline structure of graphite on the carbon surface was partially replaced by a few amounts of these supported elements deposited on the porous. The creation of a porous structure with smaller fragments broke the (002) and (101) phases and introduced an amorphous carbon in the form of a layered structure [72], as can be seen in the SEM images (Fig. 5e).

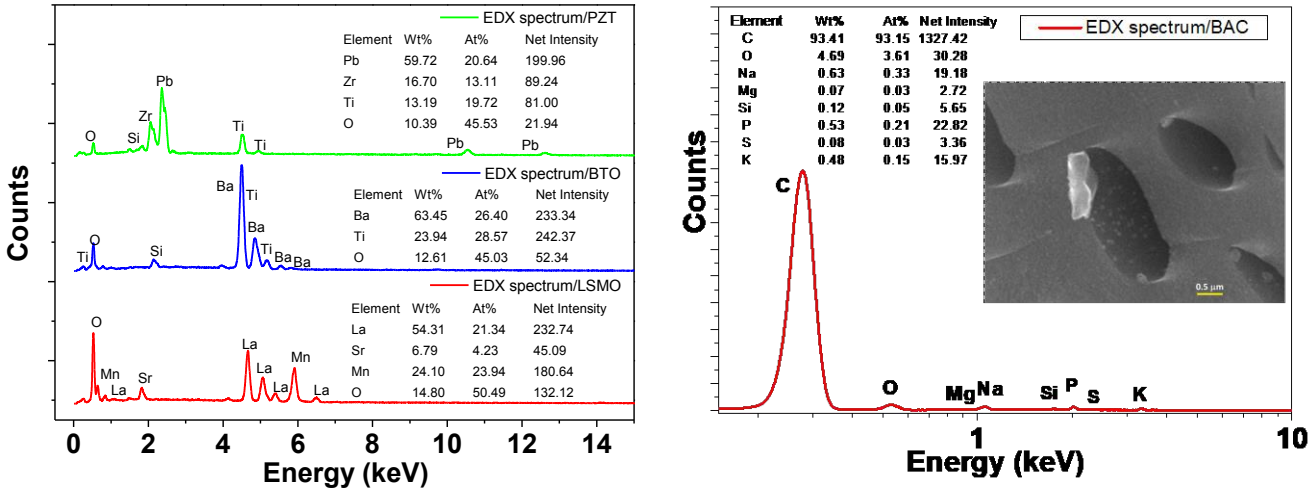

Fig. 4. EDX spectra and detailed elemental composition of LSMO, BTO, PZT (left), and BAC (right) samples. The inset in the BAC spectrum shows an SEM image of the formation of channeling pores with a small agglomerate of impurities (~1.3 μm) on its porous surface.

3.3.Morphological analysis

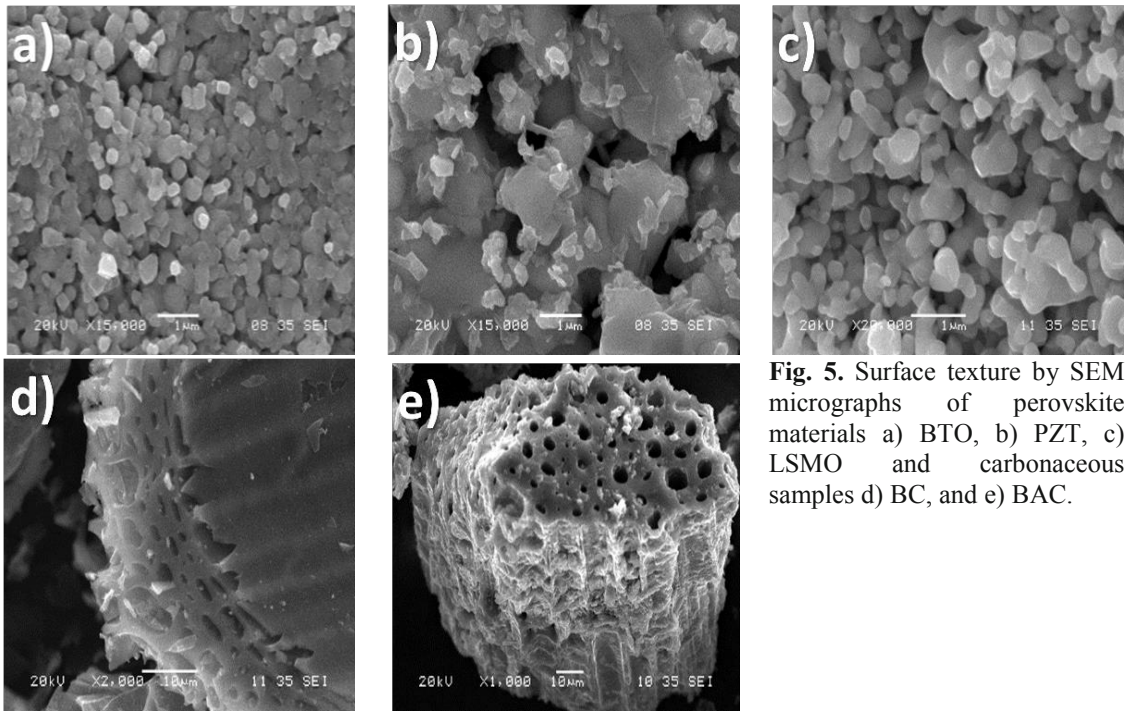

Fig. 5. Surface texture by SEM micrographs of perovskite materials a) BTO, b) PZT, c) LSMO and carbonaceous samples d) BC, and e) BAC.

Fig. 5 (a-e) shows the surface texture by SEM micrographs of BTO, PZT, LSMO, BC, and BAC. The LSMO morphology indicates aggregates with particles between 250-500 nm. The morphology of BTO has a more uniform distribution with an average particle size of 180 nm. In contrast, PZT exhibited a broad distribution of fine particles with sizes around 250 nm above micro-sized particles ranging between 1 to 2 μm. The SEM images of BC and its derivative BAC show that the external surfaces of these samples exhibited large cavities and were very irregular, indicating high porosity in both cases. However, the BAC sample exhibited more pores and well-developed cavities on its surface due to the aggressive attack of the reagent (H_3PO_4) during the pyrolysis and activation process. It helps to enhance the activated carbon's surface area and pore volume by promoting the diffusion of H_3PO_4 molecules into the pores, thereby increasing the H_3PO_4–carbon reaction and creating more pores in the activated carbon The SEM images of BC and BCA, also show that there are aggregate flat sheets with pores of the nonuniform-shaped slot. The estimate values of the pore sizes gave diameters between 1-4 μm for the BC sample and between 3-8 μm for the BAC sample, which indicates the increased in pore size after the activation.

3.4. Specific surface analysis of carbonaceous materials

For the better understanding of the specific surface and pore size of BC and BAC, nitrogen adsorption-desorption measurements were carried out at room temperature. Figure 6 shows the reversible isotherm characteristics of our BC and BAC samples. The gas adsorption-desorption pathways of both carbonaceous materials reflect a typical Type II isotherm according to the IUPAC classification, which is a characteristic of microporous adsorbents, have slit-shaped pores, and do not show any limiting adsorption at high relative pressure (P/Po) [73-75]. We found that the shape of the hysteresis loops for BC and BAC correlates with the texture of slit-shaped pores, as seen in the SEM images. Comparing the slopes associated with the desorption curves in the relative pressure range from 0.4 to 0.5, we can see that the BAC curve has a steeper slope than that of BC, which could indicate that in BAC, there is a reinforcement of particles increasing its so-called tensile strength effect. Therefore, this could prove that BAC has better mechanical properties than BC [76]. The specific surface area and pore size of carbonaceous are displayed in Table 1, indicating that BAC has much better textural characteristics than BC. The BET surface area, BJH volume of pores, micropore size, and DT micropore area of BAC are more significant than BC, proving that the carbon activation process increases these textural parameters. These parameters are reasonably comparable to those of other carbonaceous, as reported previously by Boukmouche *et al*. [61], Yakout *et al*. [62], and Zhao *et al*. [63]. Thus, the BAC gives better performance and higher attributes for electrode applications.

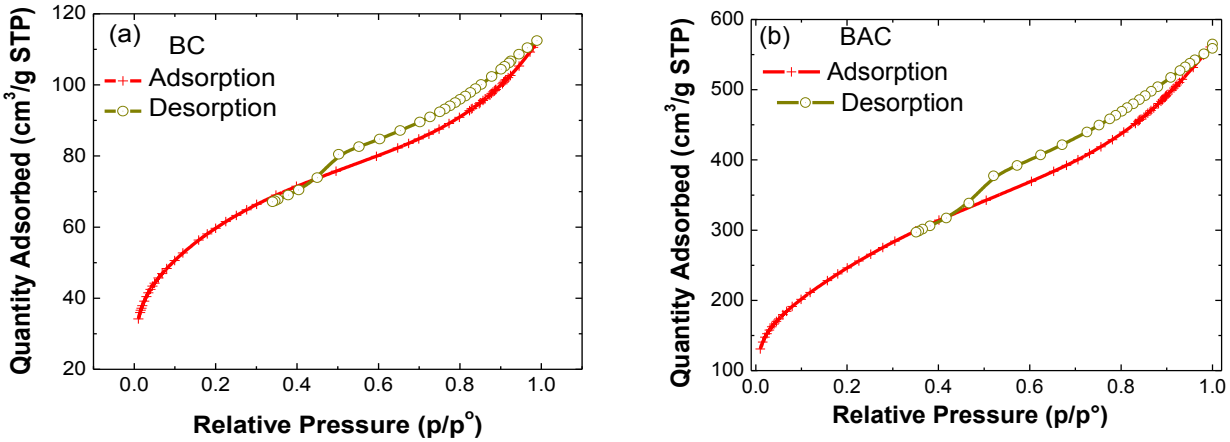

Fig. 6. Adsorption-desorption isotherm shown by (a) BC and (b) BAC samples

Table 1. Textural characteristics of carbonaceous BA and BAC samples obtained by N_2 adsorption-desorption characterization.

Parameters	Bamboo charcoal	Activated carbon
BET surface area (m^2/g)	193 ± 25	1153 ± 120
BJH volume of pores (cm^3/g)	0.14 ± 0.04	0.85 ± 0.01
Micropore size (nm)	1.27 ± 0.02	1.37 ± 0.04
DA micropore surface area (m^2/g)	0.1 ± 0.03	0.45 ± 0.01

3.5. Electrical and electrochemical studies of the LSMO+BAC electrode

To understand the charge diffusion of LSMO and LSMO+BAC, ac impedance spectroscopy measurements were carried out as described in session 2.7. Figure 7 shows the dependence of specific capacitance (C_s) as a function of frequency for as prepared LSMO and LSMO+BAC materials at an ac amplitude of 10 mV. As can be seen, the Cs decreases with increasing frequency. The C_s values of LSMO+BAC are higher than those of LSMO in the entire frequency range. This behavior happens because at lower frequencies (longer relaxation times), the electric signal penetrates the carbon pores more deeply, and a larger surface of the electrodes is involved in the charging/discharging process. The maximum specific capacitance of LSMO and LSMO+BC was calculated at 1 Hz and was found to be ~ 263 F/g and 586 F/g for, respectively. The observed Cs for LSMO is comparable to those of lanthanum-based perovskites, as reported [17,40]. However, LSMO+BAC exhibits higher C_s, which can be attributed to BAC's textural and morphology properties. The specific capacitance of activated carbons can be as high as 100 to 370 F/g [77]. The observed high specific capacitance (C_s) could be due to blending of LSMO with BAC.

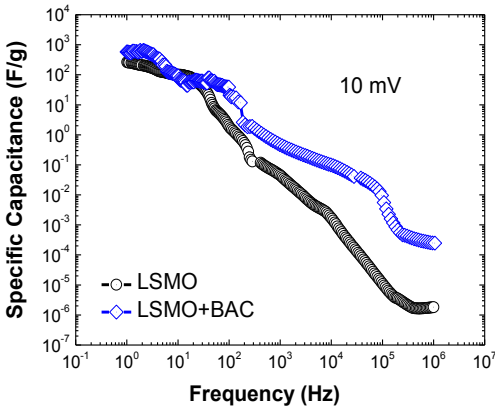

Fig. 7. Specific capacitance (C_s) as a function of frequency for LSMO and LSMO+BAC at AC amplitude of 10 mV.

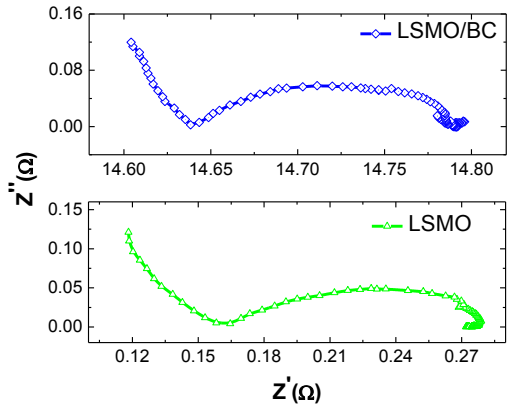

Fig. 8. Nyquist plot obtained for LSMO and LSMO+BAC electrodes at the frequency ranging from 1 Hz to 1MHz at 10 mV.

Figure 8 shows the Nyquist plots (real (Z′) and imaginary (Z″) part impedance) of LSMO and LSMO+BAC. Both electrodes exhibited semicircles with low resistances along the Z′ axis. However, even though LSMO+BAC exhibited higher resistance (~ 14.8 Ω) than LSMO (~ 0.28 Ω), its semicircle looks more symmetric, indicating that LSMO+BAC has a stable charge transfer between the bulk and the current collector contact. It is likely due to the fast movement of charge, leading to higher stability of the interface. This property is interrelated with the increased surface area and pore structure of BAC that help optimize the overall capacitance and conductivity of LSMO. Therefore, using BAC with LSMO has been found to be a suitable electrode selection for the better supercapacitors performance.

To investigate the electrochemical performance of the as-prepared LSMO and LSMO+BAC, CV and GCD measurements were carried out using a three-electrode system under relatively derated voltages as described in session 2.8. Figure 9 shows the CVs of LSMO and LSMO+BAC electrodes at different scan rates of 10, 20, 50, and 100 mV/s with a potential from -0.6 to 0.6 V (*vs.* Ag/AgCl). As can be seen, there are several features on the CV that reflect a quasi-reversibility of the electrode's reaction. First, we see that the CVs are not symmetrical for both materials. The potential of the oxidation (positive) current peaks is more favorable than that of the reduction (negative) ones. These peaks are signs of typical pseudocapacitive behavior from the faradaic redox reaction [78] in the transformation between 3^+ and 4^+ states of Mn [79]. Nevertheless, it is more evident in LSMO+BAC owing to its distorted rectangular shape CV curves. It seems that BAC has a strong effect on the electroactivity of LSMO perovskite, facilitating the redox chemistry activity of Mn^{3+} and Mn^{4+} ions, involving an improved charge transfer and indicating the influence of a typical EDLC that characterizes carbonaceous materials [80]. Second, we can also see that with increasing scan rate, from 50 to 100 mV/s, the CV curves for LSMO and LSMO+BAC exhibit a steady state, and there are no significant changes in their shape, which suggests the low resistance and stability of the electrode materials. However, the lack of symmetry of the curves is likely due to the contribution of the pseudocapacitances to the overall electrode-specific capacitances.

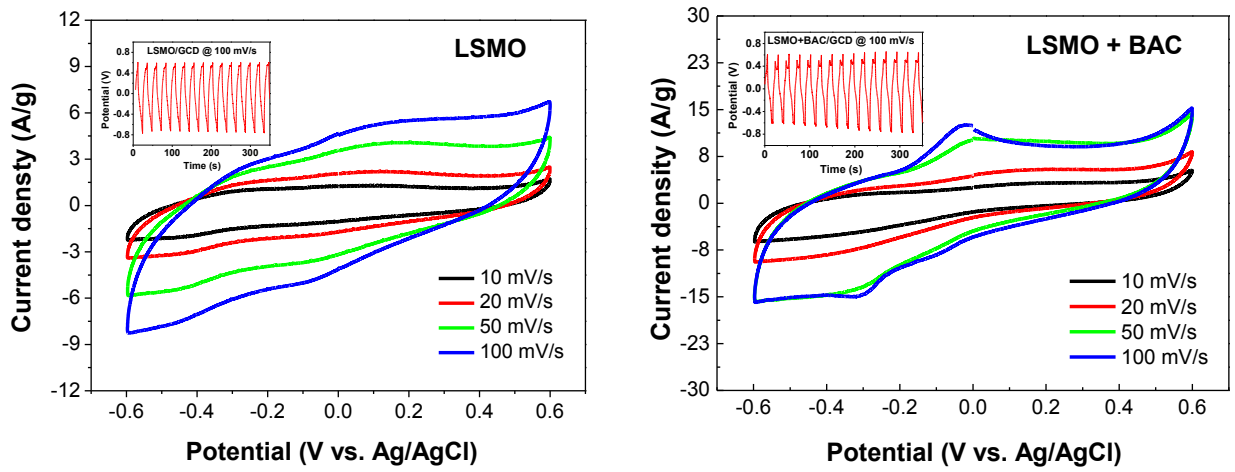

Fig. 9. Cyclic voltammograms recorded at different scan rates in 0.1 M KOH solution on LSMO (left) and LSMO+BAC (right) electrodes. Insets show the GCD curves of LSMO and LSMO+BAC at the current density of 5 A/g.

The insets in Figure 9 show the GCD profiles for LSMO and LSMO+BAC at a constant current of 5 A/g. The cycling test revealed that samples exhibit good stability during 100 cycles of length around 24 s each for both samples, suggesting that the continuous cycling does not cause appreciable aging of the electrode materials. According to Okamura *et al.* [81] and Weingarth *et al.* [82], for cycling test, only derated voltages should be applied to the capacitors to increase their lifespan. This is consistent with most of the GCD measurements performed on EDLC electrodes including metal oxides and activated carbon. It has been found that the nominal voltage of 1.4-2.0 V has been used for metal oxides in aqueous electrolytes [6,17,22,83,84], while 3.5- 4.0 V for activated carbon in inorganic electrolytes [61,72,85] for cyclic voltammetry measurements. An alternative to the cycling test for EDLC materials is the constant load or float test, which is performed by holding the electrode cell at its nominal voltage to determine the capacitance as a function of time. Nevertheless, electrode materials exposed to the constant voltage hold test with a very close or above nominal voltage for a long time could cause leakage current and instability

in the system resulting a rapid degradation of the material [82,85,86]. Thus, it is advisable to use potential windows below the nominal voltage in laboratory-scale cells to avoid stress and aging in the materials.

It is known that the C_s can be evaluated from the GCD curves and the CV curves according to Eq. 3 and 4, respectively [6, 17].

$$C_s = \frac{I\,\Delta t}{m\,\Delta V} \qquad (3) \qquad C_s = \frac{\int I_{(V)} dV}{m.\nu.\Delta V}, \qquad (4)$$

where $I(V)$, m, ν, ΔV, I, and Δt are the cathodic current, the mass of the electrode, the potential scan rate, the potential sweep window, the current of discharge and the time interval of discharge. From Eq. 3, it was found that LSMO+BAC has higher specific capacitances than its counterpart LSMO during the cycling test. Although the C_s of LSMO appears to remain almost constant (~157 to 160 F/g) that of LSMO+BAC shows a noticeable increase from ~317 to ~378 F/g and then drops slowly as the cycles progress until ~ 313 F/g , We behavior could be due the fast electron and ions transfer due to the electrochemical activation and a gradual accumulation of charges in BAC pores with increasing scan rate. However, the charge transmission has reduced possibly due to the agglomeration in the pores or impurities on the pores' surface, which is detrimental to fast ion and electron transfer, thereby reducing electrochemical performance. Despite this, the loss of capacitance is very low, and the retention is around 98% upon the cycling test. Compared to LSMO, LSMO+BAC proved higher C_s and better capacity retention. The improved cycle stability of the composite LSMO+BAC electrode can be attributed to the rapid electron transfer within the carbon porous surface area. This can be interpreted as an excellent property of LSMO+BAC for applications in devices that require long lifespan cycles and rate performance.

From CV measurements and Eq. 4, it was found that the C_s values are comparable to those of GCD measurements but decrease as the potential scan rate increases from 10 mV/s to 100 mV/s. Thus, the values varied from 373 F/g to 139 F/g on LSMO and from 811 F/g to 259 F/g on LSMO+BAC. A higher scan rate (≥ 50 mV/s) leads to either depletion or saturation of positive ions in the electrolyte inside the electrode during the electrochemical redox process, and only the outer surface can be utilized for the charge storage, reducing the capacitance. In contrast with lower scan rates (≤ 20 mV/s), high fractions of negative ions from the electrolyte will have more favorable conditions to reach the electroactive sites, thus leading to higher available capacitance [7,87]. When comparing the calculated Cs values by GCD and CV with those of ac impedance, we noticed that they are in the same order of magnitude but cannot be comparable because the capacitances in a two-electrode configuration saturate faster than in a three-electrode configuration. Hence, the C_s values rapidly decrease as the electrode thickness increases, making it challenging to obtain the specific energy values and precise contributions to specific capacitance [88]. Therefore, the measurement of the C_s by electrochemical methods is more accurate. Interestingly, at the low scan rate of 10 mV/s, LSMO+BAC exhibited a very high specific capacitance of 811 F/g. It could be competitive with other reported electrode materials such as CNT (524 F/g) [89], RuO_2xH_2O (720 F/g) [90], PANI-CNTA (1000 F/g) [91], and NiO/graphene (2584 F/g) [92]. The electrochemical results above demonstrate that LSMO+BAC is a candidate as an electrode material for supercapacitor applications.

3.6. Ferroelectric properties of BTO and PZT perovskites

To investigate the ferroelectric properties of BTO and PZT at room temperature, hysteresis loops (P-E plot) were recorded and shown in Fig. 10. Both materials exhibited healthy and saturated hysteresis

loops. However, the ferroelectricity of BTO exceeds that of the PZT. The maximum polarization at an electric field of 30 kV/cm was ~7 μC/cm^2 and ~4 μC/cm^2 for BTO and PZT, respectively. We know that dielectric materials such as BTO and PZT can store electric energy due to their polarization in an external electric field, causing a positive charge stored on one electrode and a negative on the other. This critical feature of these ferroelectric materials makes it attractive to implement them in supercapacitors for promising applications [93]. The inset in Fig 10. illustrates the stored energy density of BTO and PZT. By integrating the P-E curves [94], the values of the stored energy density were ~ 49 mJ/cm^3 for BTO and ~ 41 mJ/cm^3 for PZT.

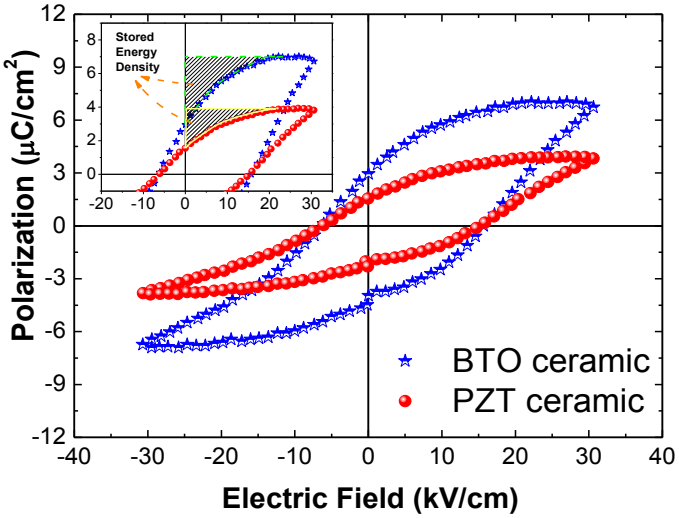

Fig. 10. Polarization (P)-electric field (E) hysteresis loops for BST and PZT perovskite ferroelectric materials at room temperature. The inset shows the corresponding energy storage density of BTO and PZT.

The observed polarization agrees well with other ferroelectric ceramics and composites, such as $Ba_{1-x}Sr_xTi_{1-y}Zr_yO_3$ [95] and PZT/PVDF [96]. Apart from good ferroelectricity and large energy storage density, BTO and PZT also have suitable dielectric and electroactive properties due their crystal structure, structural compatibility with other perovskites, and chemical stability, which are important requirements to enhance the stored energy in supercapacitors and other electrical energy storage devices.

3.7. Performance of assembled coin cell supercapacitor (CCSC) devices

In order to study the quality and compatibility of our synthesized materials, we fabricated four-coin cell supercapacitors (CCSCs) with different configurations as shown in Table 2. The performance of the SCs was investigated from the electrochemical explained in Sessions 2.11 to 2.13. The performance was investigated based on a two-electrode capacitor system (Fig. 11).

Table 2. Configurations of coin cell supercapacitors (CCSC) assembled in in the present work.

Coin Cell Supercapacitor	Configuration
CCSC #1	Cu/LSMO+BAC/BTO/cellulose/BTO/LSMO+BAC/Al
CCSC #2	Cu/LSMO+BAC/BTO/cotton/BTO/LSMO+BAC/Al
CCSC #3	Cu/LSMO+BAC/PZT/cellulose/PZT/LSMO+BAC/Al
CCSC #4	Cu/LSMO+BAC/PZT/cotton/PZT/LSMO+BAC/Al

Room temperature electrochemical measurements helped to evaluate the charge storage capability of each CCSC configuration. As can be seen from Fig. 11, all devices exhibited a rectangular shape of the CVs in a potential range of 0-0.4 V at various scan rates (10-120 mV/s), indicating a good capacitive behavior and low contact resistance. The chosen potential window of 0-0.4 V was to ensure that the repeated cycling and suppress the electrolyte's oxygen evolution reaction, which could induce a high current density and leakage current in the electrodes [97]**.** The absence of any faradic peak without a reduction-oxidation process within the voltage range demonstrates a stable charge/discharge of SC, leading to high cyclability. We can see that the CCSC devices showed slightly tilted rectangular-like shapes, indicating an effective transfer of the ions through the electrode materials. Furthermore, the current at the reversal and initial potential varies almost linearly with the scan rate, implying that the electrochemical processes at the CCSC devices are not driven by diffusion but by rather ionic migration. It draws attention to the fact that the CVs of CCSC #1 showed an excellent reversibility and higher charging current through very narrow curves of insignificant distortion at any scan rate (inset Fig 11a.) than those of the other SC configurations. This enhancement relates to the more significant adequate charge transportation between the electrodes and a high-rate capability on this device.

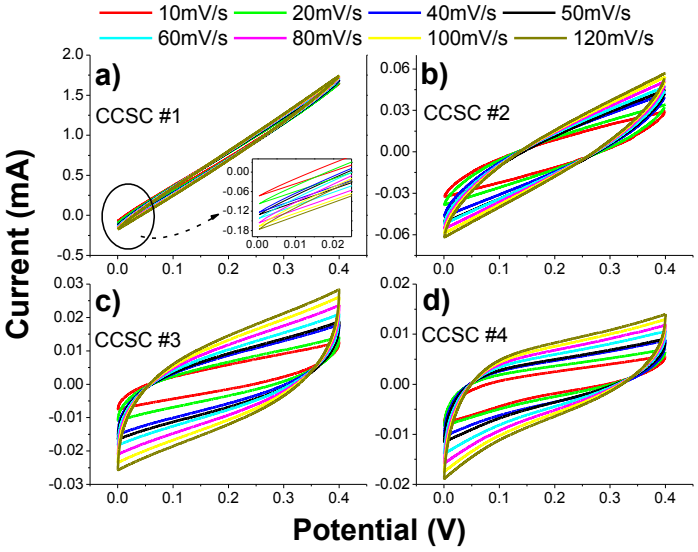

Fig. 11. Cyclic voltammograms recorded on the CCSC devices at different scan rates.

On the other hand, the influence of separator materials on the shape of CVs is manifest. Cellulose reveals an improved performance for BTO and PZT-based CCSC devices. In SC devices, the separator must provide electronic insulation between electrodes of opposite polarization to avoid short circuits and favor high conduction/mobility from the electrolyte toward the electrode surface. The roughness, surface porosity, high surface area, and electrolyte absorption are substantial advantages that cellulose fulfills and represents a green alternative for SC devices [98]. Conversely, CCSC based on cotton fabric lint separators (CCSC#2) demonstrated a weak performance compared to CCSC#1. Compared with cotton fabric lint-based CCSC devices, the cellulose-based CCSC devices exhibited higher currents at 0.4 V at all scan rates. However, this difference is more remarkable for the BTO-based CCSC devices (SC #1 and 2) than PZT-based CCSC devices (SC #3 and 4). The currents at 0.4 V and 120 mV/s for different SCs were 1.74 mA for CCSC #1, 0.057 mA for CCSC #2, 0.0283 mA for CCSC #3, and 0.0138 mA for CCSC #4. These

results indicate the beneficial impact of BTO-cellulose-based CCSC devices for faster charge propagation within the electrolyte toward the LSMO+BAC electrodes.

Figure 12 shows the C_s of the CCSC devices derived from the CV curves as a function of scanning rates, according to Eq. 4. We observed that the C_s values decrease as the potential scan rate increases. At the lowest scan rate, the C_s values were 300 F/g for CCSC #1, 6 F/g for CCSC #2, 2.7 F/g for CCSC #3, and 0.9 F/g for CCSC #4, respectively. We can see that the C_s values for CCSC #1 are higher than those of its counterpart CCSC devices. The cellulose-based separator CCSC devices generally exhibited better capacitive characteristics than the cotton fabric lint separator. This could be related to the so-called electrolyte starvation effect, which explains the dependencies of effective conductivity (σ) and density (ρ) of the separator materials in the voltage range V, resulting from the ion adsorption mechanism onto/into the porous electrodes [99]. Thus, the cellulose separators may have less influence on the starvation of ions' molar conductivity by having higher effective conductivity, consequently improving the C_s. At low scan rates ($v \leq 10$ mV/s) for systems based with BTO, there is an extreme dependence of maximum capacitance on the separator material used. In contrast, in systems based with PZT, there is only a weak dependence of maximum capacitance on the separator material. This behavior could be because the BTO/cellulose device has the appropriate combination of mobile space charge layer and high effective electrode area to get high specific capacitance. In addition, because BTO is lighter than PZT, and they both have comparable electrical resistivities (~ $4x10^9$ Ω.cm for BTO [100] and ~$1x10^9$ Ω.cm for PZT [101]), it can be expected that the ions of BTO easily and develop higher mobility within the electrolyte toward the LSMO+BAC than the ions of PZT.

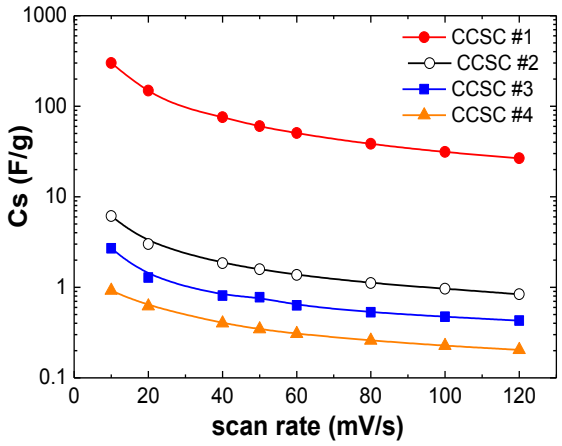

Fig. 12. Specific capacitance as a function of scan rate of CCSC devices.

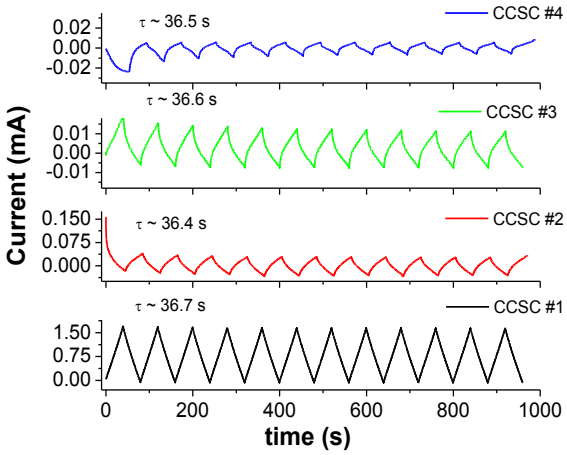

Fig. 13. Galvanostatic charge/discharge (GDC) curves of the CCSC devices.

Figure 13. shows the galvanostatic charge-discharge curves of the CCSC devices. All devices exhibited a triangular shape, but CCSC #1 displayed a symmetric charge-discharge curve corresponding to almost ideal capacitive properties. The other CCSC devices (CCSC #2-4) showed a slight drop at the beginning of the discharging step, which is more evident in those devices with cotton fabric lint separators (CCSC#2 and 4). Although, the charge-discharge time (t ~ 36-37 s) is similar to those of with the cellulose-based CCSC devices showed a higher maximum current than their cotton fabric lint counterpart. In contrast, the PZT/cellulose-based device had a lower maximum current than the BTO/cellulose-based device due to slower ion movement and diffusion in the electrolyte. On the other hand, after 12 consecutive charge-discharge cycles, the lowest retention has been showed by the CCSC #4 device (39%) compared to CCSC #3 (96%), CCSC #2 (97%), and CCSC #1 (98%). The retention rate for CCSC #4 is comparable

to that reported by Wang *et al*. for the charging capacity of lithium-ion batteries as a function of time [102].

Figure 14 shows the electrochemical impedance behavior of the tested CCSC devices in Nyquist's plots form. We can see that all SCs exhibited the typical electrochemical impedance of an EDLC, which highlights a quite steep straight line with a fast increase of Z" at the lowest frequencies and semicircular curves at the higher frequencies, indicating a favorable capacitive behavior [103]. From the shape of the depressed semicircles, the values of the equivalent series resistance or electrolyte/electrode interface resistance ($Z'(f\rightarrow\infty) = R_s$) were extracted from the x-axis intercept found to be ~ 20 Ω and 50 Ω for CCSC devices with BTO/cellulose (#1) and BTO/cotton (#2), respectively. Whereas, PZT/cellulose (#3) and PZT/cotton (#4) has series resistance of ~ 3.1 Ω and 24 Ω, respectively, which indicates the satisfactory conductivity of the electrolyte and low internal resistance of the electrodes. The R_s depend noticeably on the electroactive and separator materials used in each CCSC. As we fixed the electrode composition, current collectors, and electrolyte concentration, the variation in R_s values can be understood mainly by the different separator material parameters and electroactive materials. The difference between values of R_s can be caused primarily by the wettability of the electrolyte in the separator surface. This factor could confirm why the ionic mobility in the electrolyte contained in the cellulose improves the electrochemical properties, lowering the R_s [104, 105]. Fitting to the experimental data is depicted in solid red lines in Fig 14, and modeling to an integral equivalent circuit is shows in Fig. 15. R_s, and C_F represent the equivalent series resistor and the pseudocapacitance for the entire CCSC device. A parallel arrangement of R_F and a CPE_{dl} modeled the faradaic impedance and the double-layer capacitance of the electrode/electrolyte. At the same time, we modeled the electrodes by a parallel arrangement of R_{ele} and constant phase element (CPE_{ele}).

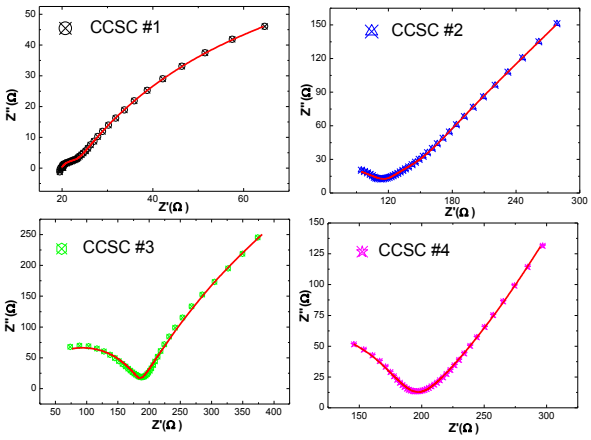

Fig. 14. Nyquist plots and modeling (solid red lines) for the electrochemical impedance of CCSC devices.

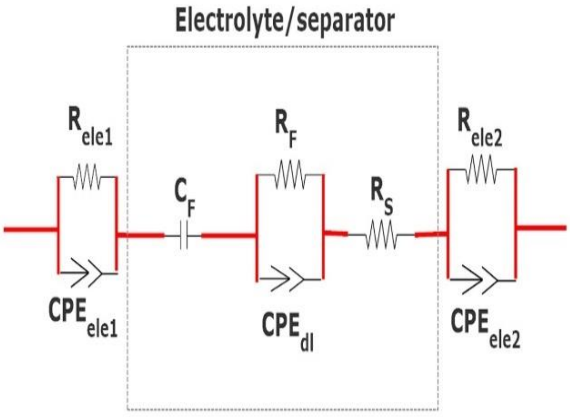

Fig. 15. Integral equivalent circuit model to represent the dynamic electrical behavior of the CCSC devices.

The dynamic electrical behavior exhibited by the CCSC devices was validated and modeled by electrochemical analyzers such as EIS Spectrum Analyser 1.0, Zview, and Zplot [106, 107]. Since, a distributed impedance response is exhibited in our heterostructures supercapacitor configurations, then a distributing factor (n) can be considered in the modeling. In consequence, to obtain a more realistic interpretation of the conduction mechanisms for the SC, constant phase elements (CPEs) are introduced. It is known that the impedance of CPE can be described as:

$$Z_{CPE} = \frac{1}{A(j\omega)^n} \qquad (4)$$

CPEs are chosen because they help to describe the rough, porous electrode surface and the formation of a double-layer interface. Following the approach for rough interfaces proposed by Martinez *et al.* [108] the real and imaginary parts of the impedance can be found as follows:

$$Z'(\omega) = \frac{R_1}{1+(\ A_1.R_1.\omega^{n_1})^2} + \frac{R_2}{1+(\ A_2.R_2.\omega^{n_2})^2} + \frac{R_3}{1+(\ A_3.R_3.\omega^{n_3})^2} + R_4 \qquad (5)$$

$$Z''(\omega) = \frac{A_1R_1^2\omega^{n_1}}{1+(\ A_1.R_1.\omega^{n_1})^2} + \frac{A_2R_2^2\omega^{n_2}}{1+(\ A_2.R_2.\omega^{n_2})^2} + \frac{A_3R_3^2\omega^{n_3}}{1+(\ A_3.R_3.\omega^{n_3})^2} + \frac{1}{\omega C} \qquad (6)$$

Where:

$$R_1 = R_{ele1},\ R_2 = R_{ele2},\ R_3 = R_F \ \ and \ \ R_4 = R_s$$

$$A_1 = CPE_{ele1},\ A_2 = CPE_{ele2},\ A_3 = CPE_{dl} \ \ and \ \ C = C_F$$

From their impedance spectroscopy results (Fig. 14), the CCSC devices showed excellent fit to Z' and Z'' plots following the Eq, 5 and Eq. 6 in concordance with the proposed equivalent circuit in Fig. 15. For CCSC #1 the parameters set were $\{CPE_{ele1},\ CPE_{ele2},\ CPE_{dl}\ , C_F,\ R_{ele1},\ R_{ele2},\ R_F, R_s\} = \{0.297\ F\ g^{-1}, 0.178\ F\ g^{-1}, 6\ F\ g^{-1}, 0.31\ F\ g^{-1}, 129.3\ \Omega, 118.2\ \Omega, 20\ \Omega$ and $18.9\ \Omega\}$ with $\{n_1,\ n_2,\ n_3\} = \{0.21, 0.23, 1\}$, respectively. However, the impedance of real systems, such as supercapacitors and batteries, is much more complex than the modeled in a circuit, and optimization of these parameters is required before making the equivalent circuit model [109]. The optimization of these parameters is our ongoing research.

Finally, to further confirm the suitability of the CCSC #1 device for practical applications, we connected two identical assembled devices in series to power a yellow LED (lowest working potential 1.75 V) as illustrated in Fig. 16. The arrangement was charged to 5 V and connected to the LED while recording the time the LED lasted on. The LED emitted bright light for over 1 minute and slowly dimmed down for approximately 2.5 more minutes, demonstrating good power and energy density. Table 3 shows the calculated energy densities and power densities of CCSC devices from the experimental data and using the Eqs. 1 and 2. From these parameters, we can see that CCSC #1 has remarkable performance, displaying an energy density of 6.7 Wh/kg and a power density of 600 W/kg, orders of magnitude higher comparable to other energy storage technologies as revisited by I. Beyers *et al*., [110]. According to Ragone's relationship, supercapacitors' energy and power densities for energy storage applications are between 1–9 Wh/kg and 10–105 W/kg, respectively [111]. Therefore, the CCSC #1 is suitable for such an application.

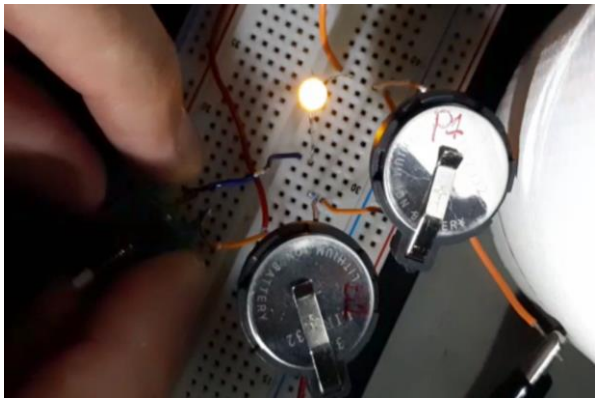

Fig. 16. Demonstration of the BTO/cellulose-based CCSC performance for practical applications by powering a yellow LED for 2.5 min.

SC configuration	Max Energy density (Wh/kg)	Max Power density (W/kg)
CCSC #1	6.7	600
CCSC #2	0.14	12.3
CCSC #3	0.06	5.4
CCSC #4	0.02	1.8

Table 3. Maxima energy density and power density of CCSC devices.

4. Conclusions

In conclusion, we have successfully synthesized and integrated several perovskite materials (LSMO, BTO, and PZT) with BAC for electrochemical supercapacitor devices using spray pyrolysis technique. Cellulose or cotton lint soaked with PVP/H_3PO_4 were used as separator/electrolyte to complete the device configurations. Supercapacitors in form of coin cell with different configurations were fabricated and tested to study the quality, compatibility, structural and chemical stability of the synthesized perovskite materials. Assembled coin cell-type devices were tested under electrochemical characterization techniques such as cyclic voltammetry, galvanostatic charge/discharge, and electrochemical impedance spectroscopy. The experimental data were modeled and represented through equivalent circuits for better understanding of electrochemical process and charge-discharge mechanisms. The results indicated that among different supercapacitor configurations, BTO/cellulose (CCSC#1) configuration showed a remarkable performance for future energy storage device due to its high specific capacitance (300 F/g), energy density (6.7 Wh/kg), power density (600 W/kg), and high retention (>95%). Finally, powering a yellow LED for several minutes illustrates the suitability for practical applications. The supercapacitors based on our approach may require further analysis and monitoring of their degradation and aging for longer life and higher performance. The feasibility study explored using perovskite materials with BAC showed promising results and could facilitate the realization of lightweight, flexible, wearable, and cost effective electrochemical hybrid supercapacitors for energy storage applications.

CRediT authorship contribution statement

Ricardo Martinez: Conceptualization, Methodology, Investigation, Writing – original draft, review and editing, Visualization, Formal analysis, Supervision. **Edwin Cruz and Shawn Zografos:** Methodology, investigation, Experiments, Writing—original draft preparation. **Joesene Soto:** Conceptualization, Methodology, investigation. **Ratnakar Palai:** Supervision, Formal analysis, Validation, Writing – review and editing**,** Funding acquisition. **Carlos Cabrera:** Supervision, Writing – review and editing, Funding acquisition.

Declaration of competing interest

The authors declare that they have no known competing financial interests or personal relationships that could have appeared to influence the work reported in this paper.

Data availability

Data will be made available on request.

Acknowledgments

The authors thank Dr. Eduardo Nicolau and Dr. Jaime Santillan, Molecular Sciences Research Center, University of Puerto Rico, San Juan, for synthesizing the cellulose separator and the adsorption isotherm measurements. Likewise, thanks to the Material Characterization Center (MCC), University of Puerto Rico, for XRD and SEM analysis. This work is supported by the NSF-PREM: Center for Interfacial Electrochemistry of Energy Materials (Grant Number 1827622).

References

[1] C. Liu, F. Li, M. Lai-Peng, H.M. Cheng, Advanced materials for energy storage, Adv. Mater., 22 (2010), pp. 28-62, https://doi.org/10.1002/adma.200903328.
[2] S.P.S. Badwal, S.S. Giddey, C. Munnings, A.I. Bhatt, A.F. Hollenkamp, Emerging electrochemical energy conversion and storage technologies, Front. Chem. 2 (2014), pp. 1-28, https://doi.org/10.3389/fchem.2014.00079.
[3] J.R. Miller, P. Simon, Materials science: electrochemical capacitors for energy management, Science. (80), 321 (2008), pp. 651-652, https://doi.org/10.1126/science.1158736.
[4] P. Simon, Y. Gogotsi, Materials for electrochemical capacitors, Nanosci. Technol. A Collect. Rev. Nat. J. 7 (2009), pp. 320-329, https://doi.org/10.1142/9789814287005_0033.
[5] Y. Cao, B. Lin, Y. Sun, H. Yang, X. Zhang, Symmetric/Asymmetric Supercapacitor Based on the Perovskite-type Lanthanum Cobaltate Nanofibers with Sr-substitution, Electrochimica Acta. 178 (2015) 398-406, https://doi.org/10.1016/j.electacta.2015.08.033.
[6] Y. Cao, B. Lin, Y. Sun, H. Yang, X. Zhang, Synthesis, structure, and electrochemical properties of lanthanum manganese nanofibers doped with Sr and Cu, Journal of Alloys and Compounds. 638 (2015) 204–213, https://doi.org/10.1016/j.jallcom.2015.03.054.
[7] X.W. Wang, Q.Q. Zhu, X.E. Wang, H.C. Zhang, J.J. Zhang, L.F. Wang, Structural and electrochemical properties of $La_{0.85}Sr_{0.15}MnO_3$ powder as an electrode material for supercapacitor, Journal of Alloys and Compounds. 675 (2016) 195–200, https://doi.org/10.1016/j.jallcom.2016.03.048.
[8] G. W. Piburn, J. T. Mefford, N. Zinni, K. J. Stevenson, S. M. Humphrey, Synthesis and charge storage properties of templated LaMnO3–SiO2 composite materials, Dalton Transactions. 46(3) (2017) 977–984, https://doi.org/10.1039/C6DT04665g.
[9] T. Shao, H. You, Z. Zhai, T. Liu, M. Li, M, L. Zhang, Hollow spherical $LaNiO_3$ supercapacitor electrode synthesized by a facile template-free method, Materials Letters. 201 (2017) 122–124, https://doi.org/10.1016/j.matlet.2017.04.143.
[10] Z. B. Cheikh, F. E. Kamel, O. Gallot-Lavallée, M. A. Soussou, S. Vizireanu, A. Achour, K. Khirouni, Hydrogen-doped $BaTiO_3$ films as solid-state electrolyte for micro-supercapacitor applications, Journal of Alloys and Compounds. 721 (2017) 276–284, https://doi.org/10.1016/j.jallcom.2017.06.019.
[11] S. F. Hussain, T.G. Subramaniam T.G, Sandeep S, L. Anup, M Samit, Supercapacitor Using a Liquid Dielectric Material, International Journal of Scientific and Research Publications, 4(11) (2018) 1-6, ISSN 2250-3153.
[12] C. Y. Chung, Y. H. Chang, Y. S. Chang, G. J. Chen, High dielectric permittivity in $Ca_{1-x}Bi_xTi_{1-x}Cr_xO_3$ ferroelectric perovskite ceramics. Journal of Alloys and Compounds. 385 (2004) 298–303, https://doi.org/10.1016/j.jallcom.2004.04.118.
[13] M. Maraj, W. Wei, B. Peng, W. Sun, Dielectric and Energy Storage Properties of $Ba_{(1-x)}Ca_xZr_yTi_{(1-y)}O_3$ (BCZT): A Review. Materials, 12(21) (2019) 3641, https://doi.org/10.3390/ma12213641.
[14] M. Meyyappan. Nanostructured materials for supercapacitors, Journal of Vacuum Science & Technology A: Vacuum, Surfaces, and Films. 31(5) (2013) 050803, https://doi.org/10.1116/1.4802772.
[15] S. P. S. Badwal, S. Giddey, C. Munnings, A. I. Bhatt, A. E. Hollenkamp, Emerging electrochemical energy conversion and storage technologies, Frontiers in Chemistry. 2 (79) (2014), https://doi.org/10.3389/fchem.2014.00079.
[16] C. Zhao, W. Zheng, A Review for Aqueous Electrochemical Supercapacitors, Frontiers in Energy Research. 3 (23) (2015),

https://doi.org/10.3389/fenrg.2015.00023.
[17] X. Lang, H. Mo, X, Hu, H. Tian, Supercapacitor performance of perovskite $La_{1-x}Sr_xMnO_3$. Dalton Trans., 46(40), (2017) 13720–13730. https://doi.org/10.1039/C7DT03134C.
[18] P. Gómez-Romero, O. Ayyad, J. Suárez-Guevara, D. Muñoz-Rojas, Hybrid organic–inorganic materials: from child's play to energy applications. Journal of Solid-State Electrochemistry. 14(11) (2010) 1939–1945, https://doi.org/10.1007/s10008-010-1076-y.
[19] B. K. Kim, S. Sy, S, A. Yu, J. Zhang, Electrochemical Supercapacitors for Energy Storage and Conversion. Handbook of Clean Energy Systems. (2015) 1–25, https://doi: 10.1002/9781118991978.hces112.
[20] B. E. Conway, *Electrochemical supercapacitors: scientific fundamentals and technological applications*. New York: Kluwer Academic/Plenum. (1999), ISBN 0-306-45736-9.
[21] T. Pandolfo, V. Ruiz, S. Sivakkumar, J. Nerkar, General Properties of Electrochemical Capacitors. Supercapacitors: Materials, Systems, and Applications. (2013) 69–109, https://doi: 10.1002/9783527646661.ch2.
[22] G. Wang, L. Zhang, J. Zhang, A review of electrode materials for electrochemical supercapacitors. Chemical Society Reviews. 41(2) (2012) 797–828, https://doi: 10.1039/c1cs15060j.
[23] Y. Zhai, Y. Dou, D. Zhao, P. F. Fulvio, R. T. Mayes, S. Dai, Carbon Materials for Chemical Capacitive Energy Storage, Advanced Materials. 23(42) (2011) 4828 – 4850, https://doi: 10.1002/adma.201100984.
[24] L-H. Su, X-G. Zhang, C-H. Mi, B. Gao, Y. Liu, Improvement of the capacitive performances for Co-Al layered double hydroxide by adding hexacyanoferrate into the electrolyte. Physical Chemistry Chemical Physics, 11(13) (2009) 2195–2202. https://doi: 10.1039/b814844a.
[25] S. T. Senthilkumar, R. K. Selvan, Y. S. Lee, J. S. Melo, J. S, Electric double-layer capacitor and its improved specific capacitance using redox additive electrolyte, J. Mater. Chem. A. 1(4) (2013) 1086–1095, https://doi: 10.1039/c2ta00210h.
[26] M. Tachibana, T. Ohishi, Y. Tsukada, A. Kitajima, H. Yamagishi, M. Murakami, Supercapacitor Using an Electrolyte Charge Storage System. Electrochemistry. 79(11) (2011) 882–886, https://doi: 10.5796/electrochemistry.79.882.
[27] S. Huang, Z. Wen, X. Zhu, Z. Gu, Preparation and electrochemical performance of Ag-doped $Li_4Ti_5O_{12}$, Electrochemistry Communications. 6(11) (2004)1093–1097, https://doi: 10.1016/j.elecom.2004.08.013.
[28] K. Naoi, 'Nanohybrid Capacitor': The Next Generation Electrochemical Capacitors. Fuel Cells. 10(5), (2010) 825–833, https://doi: 10.1002/fuce.201000041.
[29] B. Pal, S. Yang, S, S. Ramesh, V. Thangadurai, R. Jose, Electrolyte selection for supercapacitive devices: a critical review, Nanoscale Advances. 1(10) 2019) 3807–3835, https://doi: 10.1039/c9na00374f.
[30] S. Wu, W. Chen, L. Yan, Fabrication of a 3D MnO_2/graphene hydrogel for high-performance asymmetric supercapacitors, Journal of Materials Chemistry A. 2(8) (2014) 2765–2772, https://doi: 10.1039/c3ta14387b.
[31] Q.T. Qu, Y. Shi, S. Tian, Y.H. Chen, Y.P. Wu, R. Holze, A cheap asymmetric supercapacitor with high energy at high power: Activated carbon//$K_{0.27}MnO_2 \cdot 0.6H_2O$, Journal of Power Sources. 195(9) (2010) 2789–2794, https://doi: 10.1016/j.jpowsour.2009.10.108.
[32] Q.T. Qu, Y. Shi, S. Tian, Y.H. Chen, Y.P. Wu, R. Holze, A new cheap asymmetric aqueous supercapacitor: Activated carbon//$NaMnO_2$, Journal of Power Sources. 194(2) (2009) 1222–1225, https://doi: 10.1016/j.jpowsour.2009.06.068.
[33] H. Gao, F. Xiao, C. B Ching, H. Duan, High-Performance Asymmetric Supercapacitor Based on Graphene Hydrogel and Nanostructured MnO_2, ACS Applied Materials and Interfaces. 4(5) (2012) 2801–2810, https://doi: 10.1021/am300455d.
[34] P. C. Gao, A. H Lu, W. C. Li, Dual functions of activated carbon in a positive electrode for MnO_2-based hybrid supercapacitor, Journal of Power Sources. 196(8) (2011) 4095–4101, https://doi: 10.1016/j.jpowsour.2010.12.056.
[35] Y.Shlapa, S. Solopan, A. Belous, A. Tovstolytkin, Effect of Synthesis Method of $La_{1-x}Sr_xMnO_3$ Manganite Nanoparticles on Their Properties, Nanoscale Research Letters. 13(1) (2018), https://doi: 10.1186/s11671-017-2431-z.
[36] J. Marco, J. Gancedo, M. Gracia, J. Gautier, E. Ríos, F. Berry, Characterization of the Nickel Cobaltite, $NiCo_2O_4$, Prepared by Several Methods: An XRD, XANES, EXAFS, and XPS Study. Journal of Solid State Chemistry. 153(1) (2000) 74–81. https://doi: 10.1006/jssc.2000.8749.
[37] H. Arandiyan, Y. Wang, H. Sun, M. Rezaei, H. Dai, Ordered meso- and macroporous perovskite oxide catalysts for emerging applications, Chemical Communications. 54(50) (2018) 6484–6502, https://doi: 10.1039/c8cc01239c.
[38] M. Nair, H. Yen, F. Kleitz, Nanocast mesoporous mixed metal oxides for catalytic applications. Comptes Rendus Chimie. 17(7-8) (2014) 641–655, https://doi: 10.1016/j.crci.2014.04.005.
[39] S. P. Yoon, S. W. Nam, T. H. Lim, J. Han, S. A. Hong, Improved performance of $La_{0.85}Sr_{0.15}MnO_3$ cathodes by sol-gel coatings. Electrochemical Society Proceedings. (16) (2001) 485–491, https://doi: 10.1149/200116.0485PV.
[40] N. Arjun, G. T. Pan, T. C. Yang, The exploration of lanthanum-based perovskites and their complementary electrolytes for the supercapacitor applications. Results in Physics. 7 (2017) 920–926, https://doi: 10.1016/j.rinp.2017.02.013.
[41] S. Phanichphant, R. B. Heymann, Hydrothermal Synthesis of Submicron to Nano-Sized Ferroelectric Powders: Properties and Characterization. Chiang Mai University Journal of Natural Sciences, 3(2) (2004) 113–132, Retrieved from https://cmuj.cmu.ac.th/uploads/journal_list_index/41649077.pdf.
[42] H. Hayashi, Y. Hakuta, Hydrothermal Synthesis of Metal Oxide Nanoparticles in Supercritical Water. Materials. 3(7) (2010) 3794–3817, https://doi: 10.3390/ma3073794.

[43] K. C. Patil, M.S. Hedge, T. Rattan, S. T. Aruna, Chemistry of nanocrystalline oxide materials: combustion synthesis, properties, and applications, New Jersey: World Scientific. (2008) (pp. 42-60), https://doi.org/10.1142/6754.
[44] R. Branquinho, A. Santa, E. Carlos, D. Salgueiro, P. Barquinha, R. Martins, E. Fortunato, E, Solution Combustion Synthesis: Applications in Oxide Electronics, Rijeka, Croatia: InTech. Ch 15 (2016) 397-418, https://doi: 10.5772/64761.
[45] C. Falcony, M. Aguilar-Frutis, M. García-Hipólito, Spray Pyrolysis Technique; High-K Dielectric Films and Luminescent Materials: A Review. Micromachines. 9(8) (2018) 414, https://doi: 10.3390/mi9080414.
[46] N. H. Sandesh, J. V. Vijaykumar, S. M. Rajaram, Spray-pyrolysis technique for the synthesis of metal oxide nanostructures, Metal Oxides. Ch 9 (2023) 155-174, https://doi.org/10.1016/B978-0-12-824353-4.00013-0.
[47] V. K. Singh, H. N. Sah, Versatility of Spray Pyrolysis Technique for the Deposition of Carbon Thin Films. International Journal of Emerging Technologies and Innovative Research. 4(8) (2017) 312–318, Retrieved from http://www.jetir.org/papers/JETIR1708052.pdf.
[48] D. Perednis, L. J. Gauckler, Thin Film Deposition Using Spray Pyrolysis. Journal of Electroceramics, 14(2) (2005) 103–111, https://doi: 10.1007/s10832-005-0870-x.
[49] D. Maity, J. Ding, J. M. Xue, Synthesis of Magnetite Nanoparticles by Thermal Decomposition: Time, Temperature, Surfactant and Solvent Effects, Functional Materials Letters. 01(03) (2008) 189–193, https://doi: 10.1142/s1793604708000381.
[50] R. J. Deokate, R. S. Kalubarme, C. J. Park, C. D. Lokhande, Simple Synthesis of $NiCo_2O_4$ thin films using Spray Pyrolysis for electrochemical supercapacitor application: A novel approach, Electrochimica Acta. 224 (2017) 378–385, https://doi: 10.1016/j.electacta.2016.12.034.
[51] N. Shinde, R. Deokate, C. Lokhande, Properties of spray deposited Cu_2ZnSnS_4 (CZTS) thin films, Journal of Analytical and Applied Pyrolysis. 100 (2013) 12–16, https://doi: 10.1016/j.jaap.2012.10.018.
[52] Y. Sharma, R. Martinez, R. Agarwal, D. Barrionuevo, R. Katiyar, A. Kumar, R. S. Katiyar, Studies on structural, optical, magnetic, and resistive switching properties of doped $BiFe_{1-x}Cr_xO_3$ thin films. Journal of Applied Physics. 120(19), (2016) 194101, https://doi: 10.1063/1.4967993.
[53] R. Martínez, A. Kumar, R. Palai, G. Srinivasan, R. S. Katiyar, Observation of strong magnetoelectric effects in $Ba_{0.7}Sr_{0.3}TiO_3/La_{0.7}Sr_{0.3}MnO_3$ thin film heterostructures, Journal of Applied Physics. 111(10) (2012) 104104, https://doi: 10.1063/1.4717727.
[54] F. Mendoza, A. Kumar, R. Martinez, J. F. Scott, B. Weiner, R. S. Katiyar, G. Morell, Conformal coating of ferroelectric oxides on carbon nanotubes. EPL (Europhysics Letters). 97(2) (2012) 27001. https://doi: 10.1209/0295-5075/97/27001.
[55] R. Martínez, A. Kumar, R. Palai, J. F. Scott, R. S Katiyar, Impedance spectroscopy analysis of $Ba_{0.7}Sr_{0.3}TiO_3/La_{0.7}Sr_{0.3}MnO_3$ heterostructure, Journal of Physics D: Applied Physics. 44(10) (2011) 105302. https://doi: 10.1088/0022-3727/44/10/105302.
[56] R. Martinez, R. Palai, H. Huhtinen, J. Liu, J. F. Scott, R. S Katiyar, Nanoscale ordering and multiferroic behavior in $Pb(Fe_{1/2}Ta_{1/2})O_3$, Physical Review B. 82(13) (2010) 134104, https://doi: 10.1103/physrevb.82.134104.
[57] P. A. Lessing, Mixed Cation Oxide Powders via Polymeric Precursors, American Ceramic Society Bulletin. 68 (1989) 1002-1007, https://api.semanticscholar.org/CorpusID:100036217.
[58] A. Glaser, M. Ziese, Grain-boundary capacitance of $La_{0.7}Ca_{0.3}MnO_3$ films, Physical Review B. 66(9) (2002), https://doi: 10.1103/physrevb.66.094422.
[59] M. A. López-Quintela, L. E. Hueso, J. Rivas, F. Rivadulla, Intergranular magnetoresistance in nanomanganites, Nanotechnology. 14(2) (2003) 212–219, https://doi: 10.1088/0957-4484/14/2/322.
[60] V. Channu, R. Holze, E. Walker, Synthesis and characterization of $La_{0.8}Sr_{0.2}MnO_{3-\delta}$ nanostructures for solid oxide fuel cells, New Journal of Glass and Ceramics. 3(1) (2013) 29-33, https://doi: 10.4236/njgc.2013.31005.
[61] N. Boukmouche, N. Azzouz, L. Bouchama, J. Chopart, Y. Bouznit, Activated carbon derived from marine Posidonia Oceanica for electric energy storage, Arabian Journal of Chemistry. 7(3) (2014) 347–354, https://doi: 10.1016/j.arabjc.2012.12.010.
[62] S. Yakout, G. S. El-Deen, Characterization of activated carbon prepared by phosphoric acid activation of olive stones, Arabian Journal of Chemistry. 9 (2016) S1155–S1162. https://doi: 10.1016/j.arabjc.2011.12.002.
[63] W. Zhao, L. Luo, H. Wang, M. Fan, Synthesis of Bamboo-Based Activated Carbons with Super-High Specific Surface Area for Hydrogen Storage BioResources, 12(1) (2017) 1246–1262. Retrieved from https://ojs.cnr.ncsu.edu/index.php/BioRes/index.
[64] W. Chaisan, O. Khamman, R/ Yimnirun, S. Ananta, A Two-Stage Solid-State Reaction to Lead Zirconate Titanate Powders. Ferroelectrics. 356(1) (2007) 242–246, https://doi: 10.1080/00150190701512763.
[65] A. Kareiva, S. Tautkus, R. Rapalaviciute, J. E. Jorgensen, B. Lundtoft, Sol-gel synthesis and characterization of barium titanate powders, Journal of Material Science. 34, (1999) 4853–4857. https://doi: 10.1023/A:1004615912473.
[66] A. S. Gaikwad, S. S. More, R. V. Kathare, M. L. Mane, R. B. Borade,.Y. A. Vijapure, A. B. Kadam, Barium Titanate ($BaTiO_3$) synthesized by sol-gel autocombustion method, Int. Res. J. of Science & Engineering. Special Issue A5 (2018) 41–44. Retrieved from http://www.irjse.in ISSN: 2322-0015.
[67] S. Xu, Y. Moritomo, K. Ohoyama, A. Nakamura, Neutron Structural Analysis of $La_{1-x}Sr_xMnO_3$ –Variation of One-Electron

Bandwidth W with Hole Doping, Journal of the Physical Society of Japan. 72(3) (2003) 709–712, https://doi: 10.1143/jpsj.72.709.
[68] S. Maity, A. Sasmal, S. Sen, Comprehensive characterization of Ba1−xSrxTiO3: Correlation between structural and multifunctional properties, Journal of Alloys and Compounds 884 (2021) 161072, https://doi:10.1016/j.jallcom.2021.161072.
[69] M. Promsawat, A. Watcharapasorn, T. Sreesattabud, S. Jiansirisomboon, Effect of ZnO Nano-Particulates on Structure and Properties of PZT/ZnO Ceramics, Ferroelectrics. 382(1) (2009) 166–172, https://doi: 10.1080/00150190902870226.
[70] Z.Q. Li, C.J. Lu, Z.P. Xia, Y. Zhou, Z. Luo, X-ray diffraction patterns of graphite and turbostratic carbon, Carbon. 45 (2007) 1686-1695, https://doi.org/10.1016/j.carbon.2007.03.038.
[71] N. Chongtham, M. S. Bisht, O. Santosh, H. Bajwa, A. Indira, Mineral elements in Bamboo shoots and Potential role in Food Fortification, Journal of Food Composition and Analysis. 95 (2021) 103662, https://doi.org/10.1016/j.jfca.2020.103662.
[72] C. S. Yang, Y. S. Jang, H. K. Jeong, Bamboo-based activated carbon for supercapacitor applications, Current Applied Physics. 14(12) (2014) 1616–1620, https://doi: 10.1016/j.cap.2014.09.021.
[73] K. S. W. Sing, D. H. Everett, R. A. W. Haul, L. Moscou, R. A. Pierotti, J. Rouquérol, T. Siemieniewska, Reporting Physisorption Data for Gas/Solid Systems with Special Reference to the Determination of Surface Area and Porosity, International Union of Pure and Applied Chemistry. 57(4), (1985) 603–619, https://doi.org/10.1351/pac198557040603.
[74] J. C. P. Broekhoff, Mesopore Determination from Nitrogen Sorption Isotherms: Fundamentals, Scope, Limitations. Studies in Surface Science and Catalysis Preparation of Catalysts II, Proceedings of the Second International Symposium. 3 (1979) 663–684, https://doi: 10.1016/s0167-2991(09)60243-3.
[75] S. Lowell, J. E. Shields, M. A. Thomas, M. Thommes, Adsorption Hysteresis. In B. Scarlett (ed.). Characterization of porous solids and powders: surface area, pore size, and density, J. Am. Chem. Soc. 127(40) (2005) 14117, https://doi.org/10.1021/ja041016i.
[76] Z. Salleh, Z, M. Islam, M. Yusop, M. A. M.M . Idrus, Mechanical Properties of Activated Carbon (AC) Coconut Shell Reinforced Polypropylene Composites Encapsulated with Epoxy Resin, APCBEE Procedia. 9 (2014) 92–96, https://doi: 10.1016/j.apcbee.2014.01.017.
[77] L. L. Zhang, X. S. Zhao, X, Carbon-based materials as supercapacitor electrodes. Chemical Society Reviews, 38(9) (2009) 2520–2531, https://doi: 10.1039/b813846j.
[78] Z. Lin, X. Yan, J. Lang, R. Wang, L. B. Kong, Adjusting electrode initial potential to obtain high-performance asymmetric supercapacitor based on porous vanadium pentoxide nanotubes and activated carbon nanorods, Journal of Power Sources. 279 (2015) 358–364, https://doi: 10.1016/j.jpowsour.2015.01.034.
[79] J. T. Mefford, W. G. Hardin, S. Dai, K. P. Johnston, K. J. Stevenson, K. J, Anion charge storage through oxygen intercalation in $LaMnO_3$ perovskite pseudocapacitor electrodes. Nature Materials, 13(7) (2014) 726–732, https://doi: 10.1038/nmat4000.
[80] M. D. Stoller and R. S. Ruoff, Best practice methods for determining an electrode material's performance for Ultracapacitors, Energy Environ. Sci. 3 (2010) 1294–1301, https://doi: 10.1039/c0ee00074d.
[81] M. Okamura, K. Hayashi, H. Ohta, Proceedings of the 16th International Seminar on Double Layer Capacitors and Hybrid Energy Storage Devices, December 2006, Deerfield Beach, FLorida, USA, pp. 149e158.
[82] D. Weingarth, A. Foelske-Schmitz, R. Kötz, Cycle versus voltage hold - Which is the better stability test for electrochemical double layer capacitors?, Journal of Power Sources. 225 (2013) 84-88, https://doi.org/10.1016/j.jpowsour.2012.10.019.
[83] H. Xia, Y. S. Meng, G. Yuan, C. Cui, L. Lu, A Symmetric RuO_2/RuO_2 Supercapacitor Operating at 1.6 V by Using a Neutral Aqueous Electrolyte, Electrochemical and Solid-State Letters. 15 (2012) (4) A60-A63, https://doi: 10.1149/2.023204esl.
[84] N. R. Chodankar, H. D. Pham, A. K. Nanjundan, J. F. S. Fernando, K. Jayaramulu, D. Golberg, Y. K Han, D. P. Dubal, True Meaning of Pseudocapacitors and Their Performance Metrics: Asymmetric versus Hybrid Supercapacitors, Advanced Science News Nanon Micro Small. 16 (37) (2020) 2002806, https://doi: 10.1002/smll.202002806.
[85] P. Ruschhaupt, S. Pohlmann, A. Varzi, S. Passerini, Determining Realistic Electrochemical Stability Windows of Electrolytes for Electrical Double-Layer Capacitors, Batteries & Supercaps. 3 698 (2020), https://doi.org/10.1002/batt.202000009.
[86] E. Pameté, L. Köps, F. A. Kreth, S. Pohlmann, A. Varzi, T. Brousse, A. Balducci, V. Presser, The Many Deaths of Supercapacitors: Degradation, Aging, and Performance Fading, Adv. Energy Mater. 13 (2023) 2301008, https://doi.org/10.1002/aenm.202301008.
[87] K. Wang, Z. Zhang, X. Shi, H. Wang, Y. Lu, X. Ma, Temperature-dependent self-assembly of NiO/Co_3O_4 composites for supercapacitor electrodes with good cycling performance: from nanoparticles to nanorod arrays. RSC Advances. 5(3) (2015) 1943–1948, https://doi: 10.1039/c4ra14153a.
[88] G. Kim, G, I. Ryu, S. Yim, Retarded saturation of the areal capacitance using 3D-aligned MnO_2 thin film nanostructures as a supercapacitor electrode, Scientific Reports. 7(1) 8260 (2017), https://doi: 10.1038/s41598-017-09039-x.
[89] J. P. Zheng, P. J. Cygan, T. R. Jow, Hydrous Ruthenium Oxide as an Electrode Material for Electrochemical Capacitors, Journal of The Electrochemical Society. 142(8), (1995) 2699., https://doi: 10.1149/1.2050077.

[90] T. Bordjiba, M. Mohamedi, L.H. Dao, New Class of Carbon-Nanotube Aerogel Electrodes for Electrochemical Power Sources, Advanced Materials. 20(4) (2008) 815–819, https://doi: 10.1002/adma.200701498.
[91] H. Zhang, G. Cao, Z. Wang, Y. Yang, Z. Shi, Z. Gu, Tube-covering-tube nanostructured polyaniline/carbon nanotube array composite electrode with high capacitance and superior rate performance as well as good cycling stability, Electrochemistry Communications. 10(7), (2008) 1056–1059, https://doi: 10.1016/j.elecom.2008.05.007.
[92] N. A. Mala, M. A. Dar, S. Sivakumar, T. A. Dar, E. Manikandan, Review article on the performance of electrochemical capacitors when altered metals doped with nickel oxide nanomaterials, Journal of Nanoparticle Research. 24(229) (2022), https://doi: 10.1007/s11051-022-05605-1.
[93] A. Chauhan, S. Patel, R. Vaish, C. Bowen, Anti-Ferroelectric Ceramics for High Energy Density Capacitors, Materials. 8(12) (2015) 8009–8031, https://doi: 10.3390/ma8125439.
[94] A. Sasmal, S. Sen, P. S. Devi, Role of suppressed oxygen vacancies in the BiFeO3 nanofiller to improve the polar phase and multifunctional performance of poly(vinylidene fluoride), Physical Chemistry Chemical Physics. 21(11) (2019) 5974–5988. https://doi: 10.1039/c8cp07281g.
[95] B. W. Ricketts, G. Triani, A. D. Hilton, Dielectric energy storage densities in $Ba_{1-x}Sr_xTi_{1-y}ZryO_3$ ceramics. Journal of Materials Science: Materials in Electronics. 11, (2000) 513–517, https://doi: 10.1023/A:1008924703491.
[96] G. Chen, X. Lin, J. Li, J. G. Fisher, Y. Zhang, S. Huang, X. Cheng, Enhanced dielectric properties and discharged energy density of composite films using submicron PZT particles, Ceramics International. 44(13), (2018) 15331–15337, https://doi: 10.1016/j.ceramint.2018.05.181.
[97] H. Umeno, K. Kawai, D. Asakura, M. Okubo, A. Yamada, Oxygen Redox Versus Oxygen Evolution in Aqueous Electrolytes: Critical Influence of Transition Metals, Advanced Science. 9 (12) (2022) 2104907, https://doi.org/10.1002/advs.202104907.
[98] M. M. Pérez-Madrigal, M. G. Edo, C. Alemán, Powering the future: application of cellulose-based materials for supercapacitors, Green Chemistry. 18(22) (2016) 5930–5956, https://doi: 10.1039/c6gc02086k.
[99] K. Tõnurist, A. Jänes, T. Thomberg, H. Kurig, E. Lust, Influence of Mesoporous Separator Properties on the Parameters of Electrical Double-Layer Capacitor Single Cells, Journal of The Electrochemical Society, 156(4) A334 (2009), https://doi: 10.1149/1.3079339.
[100] N. Sareecha, W. A. Shah, M. Anis-Ur-Rehman, M. L. Mirza, M. Awan, Electrical investigations of $BaTiO_3$ ceramics with Ba/Ti contents under the influence of temperature, Solid State Ionics. 303 (2017) 16–23, https://doi: 10.1016/j.ssi.2017.02.003.
[101] M. A. Fraga, H. Furlan, R. S. Pessoa, M. Massi, Wide bandgap semiconductor thin films for piezoelectric and piezoresistive MEMS sensors applied at high temperatures: an overview, Microsystem Technologies. 20(1) (2013) 9–21, https://doi: 10.1007/s00542-013-2029-z.
[102] S. Wang, P. Takyi-Aninakwa, S. Jin, C. Yu, C. Fernandez, D. I. Strode, An improved feedforward-long short-term memory modeling method for the whole-life-cycle state of charge prediction of lithium-ion batteries considering current-voltage-temperature variation, Energy. 254 (part A) 124224 (2022), https://doi.org/10.1016/j.energy.2022.124224.
[103] B. A. Mei, O. Munteshari, J. Lau, B. Dunn, L. Pilon, Physical Interpretations of Nyquist Plots for EDLC Electrodes and Devices, The Journal of Physical Chemistry C. 122 (1) (2018) 194-206, https://doi: 10.1021/acs.jpcc.7b10582.
[104] B. Szubzda, A. Szmaja, M. Ozimek, S. Mazurkiewicz, Polymer membranes as separators for supercapacitors, Applied Physics A. 117(4) (2014) 1801–1809, https://doi: 10.1007/s00339-014-8674-y.
[105] S. Ahankari, D. Lasrado, R. Subramaniam, Advances in materials and fabrication of separators in supercapacitors, Mater. Adv. 3 (2022) 1472-1496, https://doi: 10.1039/d1ma00599e.
[106] A. S. Bondarenko and G. A. Ragoisha, EIS Spectrum Analyzer. (2008), http://www.abc.chemistry.bsu.by/vi/analyser/
[107] A. Ch. Lazanas, M. I. Prodromidis, Electrochemical Impedance Spectroscopy-A Tutorial, ACS Measurement Science Au. 3(3) (2023) 162-193, https://doi:10.1021/acsmeasuresciau.2c00070.
[108] R Martiınez, A Kumar, R Palai, J F Scott, R S Katiyar, Impedance spectroscopy analysis of $Ba_{0.7}Sr0_3TiO_3/La_{0.7}Sr_{0.3}MnO_3$ heterostructure, J. Phys. D: Appl. Phys., 44 (2011) 105302 (8pp), https://doi:10.1088/0022-3727/44/10/105302.
[109] P. Vadhva, J. Hu, M. J. Johnson, R. Stocker, M. Braglia, D. J. L. Brett, A. J. E. Rettie, Electrochemical Impedance Spectroscopy for All-Solid-State Batteries: Theory, Methods and Future Outlook, ChemElectroChem. 8 (2021) 1930–1947, https://doi.org/10.1002/celc.2021
[110] I. Beyers, A. Bensmann, R. Hanke-Rauschenbach, Ragone plots revisited: A review of methodology and application across energy storage technologies, Journal of Energy Storage. 73, (2023) 109097, https://doi.org/10.1016/j.est.2023.109097.
[111] M. S. Hal[er, J. C. Ellenbogen, Supercapacitors: A Brief Overview, MITRE Nanosystems Group (2006), Virginia, USA, http://www.mitre.org/tech/nanotech.